Applied Mathematical Modelling 40 (2016) 7204–7215

Contents lists available at ScienceDirect

Applied Mathematical Modelling

journal homepage: www.elsevier.com/locate/apm

Expedited constrained multi-objective aerodynamic shape optimization by means of physics-based surrogates

Slawomir Koziel[a,b], Yonatan A. Tesfahunegn[c], Leifur Leifsson[d,*]

[a] School of Science and Engineering, Reykjavik University, 101 Reykjavik, Iceland
[b] Faculty of Electronics, Telecommunications and Informatics, Gdansk University of Technology, 80-233 Gdansk, Poland
[c] Engineering Optimization & Modeling Center, Reykjavik University, Menntavegur 1, 101 Reykjavik, Iceland
[d] Department of Aerospace Engineering, Iowa State University, Ames, IA 50011, USA

ARTICLE INFO

Article history:
Received 4 August 2015
Revised 23 February 2016
Accepted 9 March 2016
Available online 24 March 2016

Keywords:
Aerodynamic shape optimization
Multi-objective design
Design space reduction
Physics-based surrogates
Kriging interpolation
Space mapping

ABSTRACT

In the paper, computationally efficient constrained multi-objective design optimization of transonic airfoil profiles is considered. Our methodology focuses on fixed-lift design aimed at finding the best possible trade-offs between the two objectives: minimization of the drag coefficient and maximization of the pitching moment. The algorithm presented here exploits the surrogate-based optimization principle, variable-fidelity computational fluid dynamics (CFD) models, as well as auxiliary data-driven surrogates (here, using Kriging). In order to permit computationally feasible construction of the Kriging models, initial design space reduction is also utilized. The design process has three major stages: (i) identification of the extreme points of the Pareto front through single-objective optimization (one objective at a time), (ii) construction of the Kriging model and initial Pareto front generation using multi-objective evolutionary algorithm (MOEA), and (iii) Pareto front refinement using response correction techniques and local response surface approximation (RSA) models. For the sake of computational efficiency, stages (i) and (ii) are realized at the level of coarse-discretization CFD model. The RSA models are also utilized to predict the angle of attack necessary to achieve the target lift coefficient, which considerably reduces the CFD simulation effort involved in the design process. Two design case studies are considered involving B-spline-parameterized airfoil shapes with 8 and 12 design variables. The 10-element Pareto front representations are obtained at the cost corresponding to just over two hundred of high-fidelity CFD model evaluations. This cost is not only considerably lower (up to two orders of magnitude) than the cost of direct high-fidelity model optimization using metaheuristics but, more importantly, renders multi-objective optimization of aerodynamic components computationally tractable even at the level of accurate CFD models.

1. Introduction

A critical aspect of contemporary aerodynamic design, especially regarding components such as aircraft wings and turbine blades is shape optimization [1,2]. The optimization process is normally executed—for the sake of reliability—at the level of high-fidelity computational fluid dynamic (CFD) simulations. Perhaps the most challenging bottleneck of automated

* Corresponding author. Tel.: +1-515-2946549.
E-mail address: leifur@iastate.edu (L. Leifsson).

http://dx.doi.org/10.1016/j.apm.2016.03.020
S0307-904X(16)30145-7/

optimization of aerodynamic components is the high computational cost of accurate CFD simulations and the fact that conventional methods require large number of such simulations to yield a satisfactory design. Therefore, hands-on techniques (mostly based on parameter sweeps guided by engineering experience) are still widespread. These methods may allow for a design improvement in a reasonable timeframe; however, obtaining truly optimum designs is hardly possible. On the other hand, design automation using numerical optimization techniques is becoming more and more popular [3–6], which is partially due to the development of computationally efficient procedures, including gradient-based algorithms [7] exploiting adjoint sensitivities [8,9], as well as various types of surrogate-based optimization (SBO) techniques [10–15]. An important advantage of SBO over conventional algorithms is the possibility of efficient global optimization (for methods with data-driven surrogates), and a substantial reduction of the design cost compared to conventional methods (for algorithms exploiting physics-based surrogates) [12].

Real-world aerodynamic shape optimization problems involve several design objectives that need to be handled simultaneously. Example design criteria include drag minimization, lift maximization, reduction of the aeroacoustic noise, control of the cross-sectional area (or the profile thickness) or a pitching moment. In many cases, it is possible to select the primary objective (e.g., drag minimization) and optimize it explicitly while handling other objectives using constraints. Another option is objective aggregation (using, e.g., weighted sum methods) [39]. In either case, the original problem can be turned into a single-objective task. On the other hand, gaining more comprehensive data about the component of interest is usually desirable, in particular, in terms of possible trade-offs between conflicting design objectives. In such cases, a genuine multi-objective optimization becomes a necessity. Multi-objective design is typically based on the concept of Pareto optimality [16]. According to a Pareto dominance relation [16] utilized for design assessment two different designs may not be comparable to each other (i.e., equally good in the multi-objective sense). Consequently, the outcome of the optimization process is sought as a set of designs representing a so-called Pareto front, i.e., the designs that are globally non-dominated in a Pareto sense [16]. Population-based metaheuristic algorithms belong to the most popular solution approaches to multi-objective optimization problems. These include multi-objective evolutionary algorithms (MOEAs) [17–19,35]. The fundamental advantage of population-based methods is their capability of generating the entire Pareto set in a single algorithm run. However, such algorithms are characterized by very high computational complexity, which is due to processing large sets (populations) of candidate solutions. Consequently, direct multi-objective optimization of high-fidelity CFD simulation models is normally impractical with these methods.

Acceleration of aerodynamic shape optimization can be achieved by means of surrogate-based optimization (SBO) [10–15]. The key concept behind reducing the computational effort in SBO is to replace the direct handling of expensive high-fidelity models by iterative construction and re-optimization of their cheap replacements, referred to as surrogates. There are two major approaches to surrogate model construction: data-driven (also called function-approximation) and physics-based modeling. According to the first approach, the surrogate is obtained by approximating the sampled high-fidelity model data (e.g., using response surface approximations, Kriging, radial basis function, and support vector machines) [10,11,15]. In the second approach, the surrogate is a suitably corrected physics-based low-fidelity model [12–14,25,26]; which is a less accurate but a computationally cheaper representation of the high-fidelity model. The physics-based low-fidelity model can be constructed based on (i) simplified physics, (ii) coarser discretization, (iii) reduced solver convergence criteria, or (iv) any combination of (i)–(iii) [12,13]. The main advantage of data-driven models is their low evaluation cost; another advantage is their good analytical properties (smoothness). A fundamental disadvantage is the high cost of training data acquisition, which might be prohibitive for high-dimensional design spaces (with over 40 design variables). In the context of design optimization, surrogate model construction and optimization is often carried out iteratively, with additional data points allocated using appropriate infill criteria that may be focused on design space exploration (for global optimization) or design space exploitation (for local modeling) [11].

The most important advantage of physics-based surrogates is their good generalization capabilities (normally, superior to that of the data-driven models). It comes from the knowledge about the system of interest embedded in the underlying low-fidelity model. Consequently, a rather limited amount of high-fidelity data is needed to ensure a good predictive power of the surrogate. In case of aerodynamic components, the low-fidelity models are usually obtained by means of coarse-discretization CFD analysis [13] often combined with simplified physics representation and/or relaxed convergence criteria. Various techniques for low-fidelity model enhancement are available, including bridge functions [27–29], calibration [25,26], space mapping [20,21,30], shape-preserving response prediction [31,32], adaptive response correction [33], and adaptive response prediction [34]. A downside of physics-based surrogates is that their evaluation cost is much higher than for data-driven models (because of the necessity to evaluate the underlying low-fidelity models). Therefore, applicability of physics-based SBO techniques is usually limited to low- and medium-dimensional design spaces where the cost of multiple low-fidelity model evaluations (while optimizing the surrogate) does not become a dominant contributor of the overall optimization cost. One of the most popular multi-fidelity SBO techniques is space mapping (SM) [20,21,30]. A SM surrogate is a composition of the low-fidelity model and simple, usually linear, transformations that re-shape the model domain (input-like SM) [21,30] to correct the model response (output-like SM) [20], or change the overall model properties (implicit-like SM) [21,30].

In this paper, we demonstrate surrogate-assisted multi-objective constrained optimization of aerodynamic components using a combination of data-driven and physics-based models. Our design approach exploits variable-fidelity CFD models, auxiliary data-driven and response surface approximation (RSA) models (both global and local), as well as multi-objective evolutionary algorithms (MOEAs). The data-driven model (here, Kriging) is constructed using sampled low-fidelity CFD

simulation data and optimized using a MOEA to yield the initial approximation of the Pareto set. Because we deal with fixed-lift design of airfoils, the angle of attack ensuring the target lift is also modeled with RSA surrogates, which reduces the computational effort of CFD simulations in the later stages of the design process. The final Pareto set is obtained using response correction techniques. Our methodology is demonstrated through two design cases involving transonic airfoils with the objectives being drag minimization and pitching moment maximization. The airfoils are parameterized using B-splines with 8 to 12 variables, depending on the test case. The total cost of the multi-objective optimization process corresponds to just over two hundred high-fidelity CFD airfoil model evaluations.

2. Multi-objective optimization methodology

In this section, we discuss a multi-objective design problem starting from a general formulation followed by a particular task considered in this work (fixed-lift design for minimum drag and maximum pitching moment). We also describe the multi-objective optimization algorithm, including a design space reduction procedure, construction of the initial Pareto set representation and its further refinement using response correction techniques and local RSA models, and finally the constraint handling procedure.

2.1. General formulation of multi-objective design optimization problem

We will denote by $\boldsymbol{x}$ the vector of design variables, and by $\boldsymbol{f}(\boldsymbol{x})=[f_1(\boldsymbol{x})\ f_2(\boldsymbol{x})\ \ldots\ f_n(\boldsymbol{x})]^T$ the vector of n high-fidelity CFD model responses. Normally, components of the vector $\boldsymbol{x}$ are parameterization variables of the aerodynamic surface (e.g., an airfoil). Examples of the model responses include the airfoil section drag coefficient $C_{d.f}$, the section lift coefficient $C_{l.f}$, or a pitching moment $C_{m.f}$.

Let $F_k(\boldsymbol{x})$, $k=1, \ldots, N_{obj}$, be a kth design objective. A typical performance objective would be to minimize the drag coefficient, in which case $F_k(\boldsymbol{x})=C_{d.f}$. Another objective would be to maximize the pitching moment, in which case $F_k(\boldsymbol{x})=1/C_{m.f}$ or $F_k(\boldsymbol{x})=-C_{m.f}$ (normally, the objectives are supposed to be minimized so the maximization problem has to be transformed into a minimization one before carrying out the design process).

If the number of objectives exceeds one, i.e., $N_{obj}>1$, then any two designs $\boldsymbol{x}^{(1)}$ and $\boldsymbol{x}^{(2)}$ for which $F_k(\boldsymbol{x}^{(1)})<F_k(\boldsymbol{x}^{(2)})$ and $F_l(\boldsymbol{x}^{(2)})<F_l(\boldsymbol{x}^{(1)})$ for at least one pair $k\neq l$, are not commensurable, i.e., none is better than the other in the multi-objective sense. We define Pareto dominance relation $\prec$ (see, e.g., Fonseca) [16], saying that for the two designs $\boldsymbol{x}$ and $\boldsymbol{y}$, we have $\boldsymbol{x}\prec\boldsymbol{y}$ ($\boldsymbol{x}$ dominates over $\boldsymbol{y}$) if $F_k(\boldsymbol{x})\leq F_k(\boldsymbol{y})$ for all $k=1, \ldots, N_{obj}$, and $F_k(\boldsymbol{x})<F_k(\boldsymbol{y})$ for at least one k. The goal of the multi-objective optimization is to find a representation of a so-called Pareto front (of Pareto-optimal set) X_P of the design space X, such that for any $\boldsymbol{x}\in X_P$, there is no $\boldsymbol{y}\in X$ for which $\boldsymbol{y}\prec\boldsymbol{x}$ (Fonseca) [16]. Effectively, the Pareto front gives us information about the best possible trade-offs between the competing objectives, such as the minimum drag for a given value of the lift coefficient. Having reasonable representation of the Pareto front is therefore indispensable in making various design decisions. However, it should be emphasized that a decision making process, i.e., selection of a specific design from a number of alternatives contained in the Pareto front (e.g., based on the preferences concerning, among others, importance of particular objectives) is beyond the scope of this work. Here, we merely consider the methodology for obtaining the Pareto front itself.

The optimization procedure exploited in this paper relies on two types of CFD models: the original high-fidelity model $\boldsymbol{f}$ representing the component of interest with sufficient accuracy, and its low-fidelity counterpart $\boldsymbol{c}$. Utilization of the low-fidelity model allows for reducing the computational cost of the design optimization process as explained later in this section. The low-fidelity model is based on coarse-discretization CFD simulations (its detailed setup is discussed in Section 3.2), which allows for faster evaluation at the cost of some accuracy degradation. While most of the operations in the design procedure outlined below are carried out using the low-fidelity model, we are ultimately interested in obtaining the Pareto set for the high-fidelity model. Consequently, a refinement procedure is necessary to "elevate" the Pareto-optimal designs to the high-fidelity model level (cf. Section 2.5).

2.2. Fixed-lift transonic airfoil design

In this work, we consider lift-constrained transonic airfoil design assuming two design objectives: $F_1(\boldsymbol{x})=C_{d.f}(\boldsymbol{x})$ – minimization of the drag coefficient, and $F_2(\boldsymbol{x})=-C_{m.f}(\boldsymbol{x})$ – maximization of the pitching moment. The operating conditions are determined by a given Mach number M_∞ and a Reynolds number Re_c (based on the airfoil chord length c). The design optimization process is subjected to two constraints: an inequality constraint $g_1(\boldsymbol{x})=t_{minx}-t_x(\boldsymbol{x})\leq 0$ where t_{minx} is a minimum thickness at a chordwise location x, $0\leq x\leq c$, and t_x is the thickness of the airfoil at the chordwise location x, and an equality constraint $g_2(\boldsymbol{x})=C_{l.target}(\boldsymbol{x})-C_l=0$, where $C_{l.target}$ is the target lift coefficient to be maintained and C_l is the lift coefficient of the current design. The angle of attack α is a dependent variable adjusted to achieve $C_{l.target}$ for any given airfoil geometry $\boldsymbol{x}$.

2.3. Design space reduction

An important component of the multi-objective optimization methodology considered in this work is a data-driven model (here, implemented using Kriging interpolation) [10,11]. The initial approximation of the Pareto front is obtained by

optimizing it using a multi-objective evolutionary algorithm (cf. Section 2.4). However, it is impractical to attempt construction of the Kriging model in the entire design space because of a large number of training samples required to ensure a reasonable accuracy of the surrogate. In higher-dimensional design spaces it might be even prohibitive to acquire the training data. Therefore, the first step of the optimization procedure is to reduce the design space so that the Kriging model is only constructed in the region containing the Pareto optimal designs.

The initial box constraints (lower and upper bounds of the design variables) are normally set without much insight into the location of the optimum designs; consequently, the initial design space is rather large. On the other hand, the Pareto optimal-set usually resides in a small region of the space. The location of this region can be estimated through single-objective optimizations with respect to each design goal. Consider $\boldsymbol{l}$ and $\boldsymbol{u}$ as initial lower/upper bounds for the design variables. Let

$$\mathbf{x}_c^{*(k)} = \arg\min_{\boldsymbol{l}\le\boldsymbol{x}\le\boldsymbol{u}} F_k(\mathbf{c}(\mathbf{x})), \tag{1}$$

where $k=1, \ldots N_{obj}$, is an optimal design of the low fidelity-model $\boldsymbol{c}$ with respect to the kth objective.

These extreme points of the Pareto optimal-set are denoted by $\boldsymbol{x}_c{}^{*(k)}$. The boundaries of the reduced design space can be then defined as $\boldsymbol{l}^*=\min\{\boldsymbol{x}_c{}^{*(1)}, \ldots, \boldsymbol{x}_c{}^{*(Nobj)}\}$ and $\boldsymbol{u}^*=\max\{\boldsymbol{x}_c{}^{*(1)}, \ldots, \boldsymbol{x}_c{}^{*(Nobj)}\}$. The reduced space is usually orders of magnitude (volume-wise) smaller than the initial one, which makes the generation of an accurate Kriging model possible at a reasonably low computational expense. Although some of the Pareto optimal solutions might fall outside the reduced design space; the majority of them are normally accounted for assuming that the objectives are continuous functions of the design variables and the Pareto front is a connected set.

2.4. Initial Pareto set approximation

The data-driven surrogate is established in the reduced design space (described in the previous section). We denote this model as $\boldsymbol{s}_{KR}$. In order to reduce the overall cost of the design optimization process the model is identified using sampled low-fidelity CFD simulation data. We use Latin Hypercube Sampling [22] as the design of experiments technique. The surrogate model itself is constructed by means of Kriging interpolation [10,11]. The Kriging model $\boldsymbol{s}_{KR}$ interpolates the all the figures of interest, specifically, the drag coefficient, the pitching moment, but also the angle of attack that gives the required value of the lift coefficient.

The set of designs representing the initial Pareto front for the problem at hand is generated by optimizing the surrogate model $\boldsymbol{s}_{KR}$, using multi-objective evolutionary algorithm (MOEA). Here, we utilize a standard multi-objective evolutionary algorithm working with floating point representation, and equipped with fitness sharing, Pareto-dominance tournament selection, and mating restrictions [16]. Note that the high-fidelity model $\boldsymbol{f}$ is not evaluated until this stage of the optimization process.

A separate note is necessary regarding constraint handling. As mentioned in Section 2.2, we have one inequality constraint (concerning the airfoil thickness) and a single equality constraint (concerning the target lift coefficient). The second constraint is not handled directly because all the data points acquired for construction of the RSA model exhibit the target lift (i.e., the angle of attack is already adjusted as explained in Section 2.F to ensure that $c_2(\boldsymbol{x})=0$). Thus, the second constraint is implicitly satisfied (approximately, of course) for the entire region of validity of the RSA model. Handling of the first constraint is realized as follows at the level of solution assessment: a penalty factor is added for infeasible individuals causing them to die out in the course of the algorithm run. Furthermore, creation of infeasible individuals is suppressed at the level of solution crossover and mutation (the operations are performed repeatedly until the constraint is satisfied).

2.5. Pareto set refinement

The initial Pareto set obtained by optimizing the Kriging surrogate with the MOEA corresponds to the low-fidelity model. It needs to be "elevated" to the high-fidelity model level in order to constitute the final solution of the design problem. It is realized using a refinement procedure that works as follows. We select K designs from the initial Pareto set: $\boldsymbol{x}_s{}^{(k)}$, $k=1, \ldots, K$. The solutions are selected to provide uniform coverage of the initial Pareto front. These designs are subsequently refined using SBO to find the Pareto-optimal designs at the high-fidelity model $\boldsymbol{f}$. The description of the SBO scheme given below assumes two design objectives: F_1 and F_2; however, the procedure can be generalized to any number of objectives. For each $\boldsymbol{x}_s{}^{(k)}$, the corresponding high-fidelity model solution $\boldsymbol{x}_f{}^{(k)}$ is found using the output space mapping (OSM) algorithm of the form [20]

$$\mathbf{x}_f^{(k.i+1)} = \arg\min_{\mathbf{x}, F_2(\mathbf{x})\le F_2(\mathbf{x}_s^{(k.i)})} F_1\left(\mathbf{s}_P^{(k)}(\mathbf{x}) + [\mathbf{f}(\mathbf{x}_s^{(k.i)}) - \mathbf{s}_P^{(k)}(\mathbf{x}_s^{(k.i)})]\right), \tag{2}$$

where $\boldsymbol{x}_f{}^{(k.i)}$ is the ith approximation of $\boldsymbol{x}_f{}^{(k)}$. Here, $\boldsymbol{s}_P{}^{(k)}$ is a local RSA model of the low-fidelity model $\boldsymbol{c}$, established in the vicinity of $\boldsymbol{x}_s{}^{(k)}$, using evaluation of $\boldsymbol{c}$ at $\boldsymbol{x}_s{}^{(k)}$, $\boldsymbol{c}(\boldsymbol{x}_s{}^{(k)})$, and at $2n$ perturbations around it (we use the so-called star-distribution design of experiments) [21]. The model itself is a second-order polynomial without mixed terms [38], which allows for capturing the low-fidelity model curvature using a small number of training samples. The perturbation size is determined relative to the Pareto front span (referred back to the design space; here, we use 10 percent of the parameter ranges along the front).

It should be noted that formulation (2) aims at improving the first objective F_1 for each $\boldsymbol{x}_f^{(k)}$ without degrading F_2. The utilization of OSM ensures perfect alignment of the surrogate model $\boldsymbol{s}_{KR}$ with the high-fidelity model at the beginning of each iteration of (2). Typically, 2 to 3 iterations are required to find the desired high-fidelity model solutions $\boldsymbol{x}_f^{(k)}$. The OSM-driven refinement procedure is repeated for all K chosen samples. One should emphasize that the evaluation of the high-fidelity model $\boldsymbol{f}$ is performed only during the refinement step. The termination condition for the refinement procedure is based on the maximum distance between two subsequent sets of selected designs (i.e., $\boldsymbol{x}_f^{(k)}$, $k=1, \ldots, K$) obtained in two consecutive iterations of the procedure. Here, we use the threshold of 2 drag counts.

2.6. Optimization algorithm

The components described in the previous sections are put together into a multi-objective design optimization algorithm which can be summarized as follows:

1. Perform design space reduction;
2. Sample the design space and acquire the low-fidelity model data;
3. Construct the Kriging interpolation model $\boldsymbol{s}_{KR}$;
4. Obtain the Pareto front by optimizing $\boldsymbol{s}_{KR}$ using MOEA;
5. Refine selected elements of the Pareto front, $\boldsymbol{x}_s^{(k)}$, to obtain corresponding high-fidelity model designs $\boldsymbol{x}_f^{(k)}$ (cf. Section 2.5).

It should be emphasized that the high-fidelity model $\boldsymbol{f}$ is not evaluated until the refinement stage (Step 5). Furthermore, the cost of finding the high-fidelity model Pareto-optimal set is only about three evaluations of the high-fidelity model per design. In case of considerable discrepancy between $\boldsymbol{s}_{KR}$ and $\boldsymbol{f}$ it is possible to enhance (precondition) the Kriging model by aligning it with the high-fidelity model at certain (usually small) number of designs using space mapping [21]. In particular, the surrogate model response can be subject to transformation such as $\boldsymbol{s}_{KR}(\boldsymbol{x}) \rightarrow A(\boldsymbol{x})\boldsymbol{s}_{KR}(\boldsymbol{x})+D(\boldsymbol{x})$ with the A and D being, e.g., linear or affine functions of $\boldsymbol{x}$ with the parameters extracted by solving appropriate regression problems such as $A(\boldsymbol{x}_{SM}^{(k)})\boldsymbol{s}_{KR}(\boldsymbol{x}_{SM}^{(k)})+D(\boldsymbol{x}_{SM}^{(k)})=\boldsymbol{f}(\boldsymbol{x}_{SM}^{(k)})$, for $k=1, \ldots, N_{SM}$, where $\boldsymbol{x}_{SM}^{(k)}$ are the training points selected for preconditioning purposes.

2.7. Fixed-lift condition control

For fixed-lift constrained problems, a possible approach is to update the angle of attack directly in the flow solver to maintain the required value of the lift coefficient. However, this approach is not practical since most commercial flow solvers are proprietary. Another approach, utilized in this work, is to change angle of attack outside the flow solver. An algorithm is developed that finds the required angle of attack for the given target lift and then the optimization is performed at that particular angle of attack. Two separate procedures are used at two stages of the multi-objective optimization process: (i) before design space reduction while performing the single-objective optimization, and (ii) after yielding the initial Pareto set approximation. The first procedure is referred to as a prior-algorithm; the second one is called the post-algorithm.

The prior-algorithm can be summarized, for any design $\boldsymbol{x}$, as follows:

1. Initialize: $C_{l.target}$, α_0, $\Delta\alpha$, ε, and *maxiter*.
2. Execute the flow solution at $\alpha=\alpha_0$; IF $||C_l - C_{l.target}|| \leq \varepsilon$ accept α and go to 7; OTHERWISE continue.
3. Execute the flow solution at $\alpha=\alpha_0+\Delta\alpha$; IF $||C_l - C_{l.target}|| \leq \varepsilon$ accept α and go to 7; OTHERWISE continue.
4. Set $j=1$.
5. Construct a linear model to predict α based on simulation results at Steps 2 and 3.
6. Execute the flow solution at α; IF $||C_l - C_{l.target}|| \leq \varepsilon$ OR $j=$*maxiter* accept α and go to 7; ELSE set $j=j+1$ and go to Step 5.
7. END.

Here, α_0, $\Delta\alpha$, ε, and *maxiter* are the initial angle of attack, the perturbation of angle of attack for the linear model, the tolerance for the target lift, and the maximum number of iterations to obtain the target lift, respectively.

As described in Section 2.6, a data-driven surrogate model $\boldsymbol{s}_{KR}$ is constructed in the reduced design space using the sampled low-fidelity model data with the prior algorithm utilized to control the lift coefficient. The low-fidelity model database created on this occasion is exploited for lift control in the remaining parts of the optimization process. As explained in Section 2.4, the Kriging surrogate $\boldsymbol{s}_{KR}$ models not only the aerodynamic forces but also the angle of attack corresponding to the target lift coefficient.

The post algorithm assumes (locally) linear relationship between the lift coefficient and the angle of attack. Both a good initial value of the angle of attack and the "slope" $L=dC_l/d\alpha$ is restored from the aforementioned database by looking up the design that is closest to the currently considered one. This allows for a substantial reduction of the number of CFD simulations required to obtain a required lift coefficient value. The database will be denoted as X_B; it consists of the data sets $\{\boldsymbol{x}_B^{(k)}, \alpha_B^{(k)}, L_B^{(k)}\} \in X_B$, $k=1, \ldots, N_B$, where $\boldsymbol{x}_B^{(k)}$ is a design vector, $\alpha_B^{(k)}$ is the angle of attack ensuring $C_{l.target}$, and $L_B^{(k)}$ is the slope $dC_l/d\alpha$ at $\boldsymbol{x}_B^{(k)}$.

The post-algorithm works, for any design $\boldsymbol{x}$, as follows (in the description below, we use notation $\boldsymbol{s}_{KR.\alpha}(\boldsymbol{x})$ to denote the predicted angle of attack that give the required lift coefficient for the design $\boldsymbol{x}$):

1. Find $k_{\min} = \min\{k = 1, \ldots, N_B : \|\boldsymbol{x} - \boldsymbol{x}_B^{(k)}\|\}$.
2. Set $j = 1$.
3. Set the initial angle of attack $\alpha = \boldsymbol{s}_{KR.\alpha}(\boldsymbol{x})$.
4. Execute the flow solution at α.
5. Calculate $\Delta\alpha = (C_{l.target} - C_l)/L_B^{(k\min)}$.
6. Execute the flow solution at $\alpha \leftarrow \alpha + \Delta\alpha$.
7. If $\|C_l - C_{l.target}\| \le \varepsilon$ return α; ELSE go to Step 5.

Because of using the information stored in the database, the post-algorithm normally needs just two flow solutions to identify the required value of the angle of attack (although the procedure above is generic and can be iterated if necessary). In contrary to this, the prior algorithm requires, on average, four fine model evaluations. This results in substantial computational savings especially that the post-algorithm can also be used for the high-fidelity model evaluations.

3. Verification case studies

The methodology presented in Section 2 is illustrated using two design case studies involving transonic airfoils in fixed-lift condition. In both cases, two conflicting objectives are considered: drag minimization and pitching moment maximization. The specific problems considered here are formulated in Section 3.1. The CFD airfoil models utilized in the optimization process are described in Section 3.2, whereas numerical results and their discussion are provided in Section 3.3.

3.1. Transonic airfoil shape design problem formulation

We consider re-design of the RAE 2822 transonic airfoil shape considering two objectives: maximization of the pitching moment coefficient and minimization of the section drag coefficient. In other words, we have, $F_1(\boldsymbol{x}) = -C_{m.f}$ and $F_2(\boldsymbol{x}) = C_{d.f}$. In the two demonstration cases, the free-stream Mach number is fixed at $M_\infty = 0.734$ with the section lift coefficient constraint $C_{l.target}$ set to 0.824 for both cases (these operating and target condition are selected based on benchmark cases for aerodynamic shape optimization, for more details see, for example, Leifsson et al. [40] and Tesfahunegn et al.) [41].

The airfoil shape is parameterized using B-spline curves. The design variable vector is $\boldsymbol{x} = \boldsymbol{p}$, where $\boldsymbol{p}$ is a vector of the size $m \times 1$, with m being the total number of control parameters. The airfoil surfaces are written in parametric form as [36]

$$x(t) = \sum_{i=1}^{n+1} X_i N_{i,k}(t), \tag{3a}$$

$$z(t) = \sum_{i=1}^{n+1} Z_i N_{i,k}(t), \tag{3b}$$

where (x, z) are the Cartesian coordinates of the surface, $N_{i,k}$ is the B-spline basis function of order k, (X_i, Z_i) are the coordinates of the B-spline control polygon, and $n + 1$ is the total number of control points. Note that the surface description with (3a) and (3b) is continuous. The control points are used as design variables and allowed only to move freely up and down as shown in Fig. 1 (in this figure—for the sake of simplicity—we only show the upper surface of the airfoil). Thus, we have the Z_i coordinates of the control points as the design variables, i.e., $\boldsymbol{x} = \boldsymbol{p} = [Z_1\ Z_2\ \ldots\ Z_{n+1}]^T$, and the corresponding X_i coordinates are fixed during the optimization process. To test the proposed approach we use 8 design variables for the first case and 12 for the second case. For all cases, the upper and lower bounds for the design variables are set 0.1 and −0.1, respectively.

Two thickness constraints are imposed in both cases: $t(0.2) \ge 0.75 \cdot t(0.2)_{baseline}$, and $t(0.8) \ge 0.75 \cdot t(0.8)_{baseline}$, where $t(0.2)$ and $t(0.8)$ are airfoil thicknesses at $x = 0.2$ and $x = 0.8$, respectively, and $t(0.2)_{baseline}$ and $t(0.8)_{baseline}$ are the thicknesses of the baseline airfoil. Additionally, the lift-constraint is introduced ($C_{l.target} = 0.824$) and handled as explained in Section 2.7. In the pitching moment maximization, drag constraint ($C_{d.max} = 0.0190$) is introduced; it is handled using a penalty function approach.

3.2. CFD models

The flow is assumed to be steady, viscous, and turbulent. The compressible Reynolds-Averaged Navier-Stocks (RANS) equations are taken to be the governing fluid flow equations with Spalart-Allmaras turbulence model. The grids are generated using the hyperbolic C-mesh of Kinsey and Barth [37]. The farfield is set 100 chords away from the airfoil surface and the grid points are clustered at the trailing and leading edge of the airfoil to give a minimum stream-wise spacing of $0.001 \times$ chord length. The distance from the airfoil surface to the first node is $5 \cdot 10^{-5} \times$ chord length. The example grid is shown in Fig. 2.

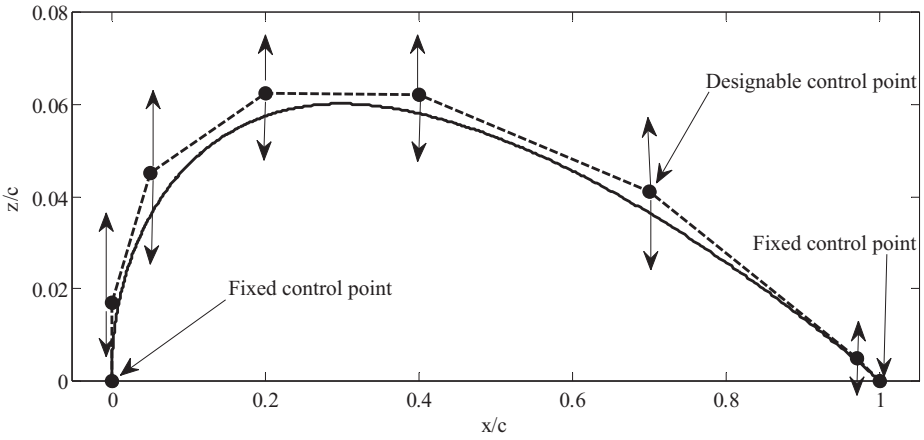

Fig. 1. Example B-spline parameterization for the upper surface of an airfoil. The designable control points are restricted to vertical movements only.

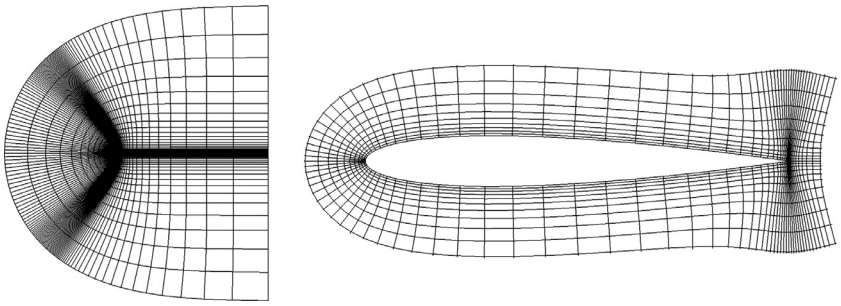

Fig. 2. Example hyperbolic C-grid showing a farfield view (left) and a view close to the airfoil surface (right).

Table 1
Grid convergence study of the high-fidelity CFD model for RAE 2822 at $M_\infty = 0.734$ and $\alpha = 2.79$ deg.

Grid size	C_l (cts)	C_d (cts)
255×32 (~8000 cells)	78.64	185.95
511×64 (~33,000 cells)	79.84	187.86
1023×128 (~132,000 cells)	80.40	190.20
2047×256 (~526,000 cells)	80.56	190.78
4095×512 (~2,101,000 cells)	80.53	190.58

The free-stream Mach number, static pressure, and angle of attack are prescribed at the farfield boundary. The flow solver is of implicit density-based formulation and the fluxes are calculated by an upwind-biased second-order spatially accurate Roe flux scheme. Asymptotic convergence to a steady-state solution is obtained for each case. The solution convergence criterion for the high-fidelity model is the one that occurs first of the following: a reduction of all the residuals by six orders, or a maximum number of iterations of 1800. Numerical fluid flow simulations are carried out using the computer code FLUENT [23,24].

A grid convergence study was performed using the RAE 2822 airfoil at a Mach number of $M_\infty = 0.734$ and an angle of attack of $\alpha = 2.79$ deg. The study, shown in Table 1, revealed that roughly 520,000 mesh cells are needed for mesh convergence, and that particular mesh was used for the high-fidelity model. The grid has 1280 points in the streamwise direction and 512 points in the direction normal to the airfoil surface. The region behind the airfoil to the farfield contains 256 points. Although the flow equation residuals are not converged after 2000 iterations, the lift and the drag coefficients are converged within 1800 iterations. Therefore, the maximum number of iterations is set to 1800. The overall simulation time of the high-fidelity model is around 120 minutes. The same is true for the other meshes, the flow equation residuals are not converged after 2000 iterations. However the lift and drag coefficients are converged within 500 to 2000 iterations.

The low-fidelity CFD model is constructed in the same way as the high-fidelity model, but with a coarser computational mesh and relaxed convergence criteria. For the low-fidelity model, we use the coarse mesh in the grid study presented in Table 1, with roughly 8,000 mesh cells. The flow solution history for the low-fidelity model, shown in Fig. 3(a), indicates that the lift and drag coefficients are nearly converged after 400 to 500 iterations. The maximum number of iterations is set

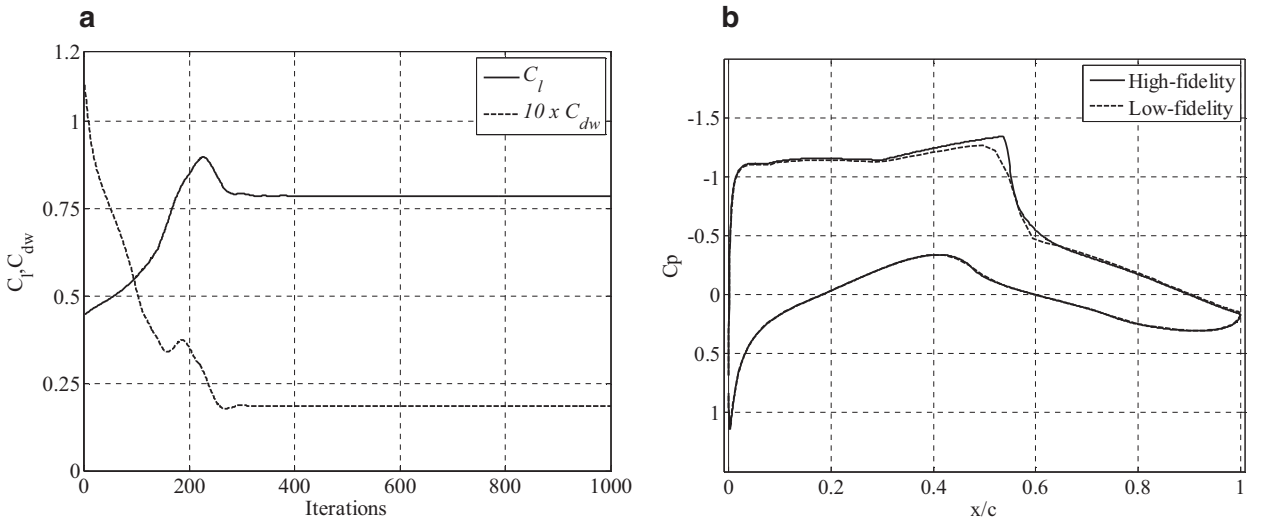

Fig. 3. Simulation results for RAE 2822 at a Mach number of $M_\infty = 0.734$ and an angle of attack of $\alpha = 2.79°$: (a) the evolution of the lift and drag coefficients obtained by the low-fidelity model; (b) a comparison of the pressure distributions obtained by the high- and low-fidelity models.

to 500 for the low-fidelity model. Hence, the overall simulation time is around 4 minutes on the same 4 processors as the high-fidelity model. Consequently, in this case study, the high-to-low simulation ratio is around 30.

A comparison of the pressure distributions, shown in Fig. 3(b), indicates that the low-fidelity model, in spite of being based on much coarser mesh and reduced flow solver iterations, captures the main features of the high-fidelity model pressure distribution quite well. The biggest discrepancy in the distributions is around the shock on the upper surface, leading to an under estimation of both lift and drag (Table 1).

3.3. Numerical results: design case I

The extreme point of the Pareto front obtained at the level of the low-fidelity CFD model obtained for the first design case (B-spline parameterization with 8 design variables at fixed lift, $C_{l.target} = 0.824$) are as follows: drag minimization, $\boldsymbol{x}_c^{*(1)} = [0.0227\ 0.0490\ 0.0703\ 0.0540\ -0.0269\ -0.0479\ -0.0318\ 0.0054]^T$, $C_l = 0.8239$, $C_d = 0.0129$, $C_m = -0.1099$, and pitching moment maximization $\boldsymbol{x}_c^{*(2)} = [0.0205\ 0.0409\ 0.0666\ 0.0315\ -0.0269\ -0.0479\ -0.0495\ 0.0032]^T$, $C_l = 0.8240$, $C_d = 0.0190$, $C_m = -0.0465$. The reduced design space (according to Section 2.2) is therefore defined by the following bounds: $\boldsymbol{l}^* = [0.0205\ 0.0409\ 0.0666\ 0.0315\ -0.0269\ -0.0479\ -0.0495\ 0.0032]^T$ and $\boldsymbol{u}^* = [0.0227\ 0.0490\ 0.0703\ 0.0540\ -0.0269\ -0.0479\ -0.0318\ 0.0054]^T$. It is over 10^{14} times smaller (volume-wise) than the original space. The extreme points were obtained using the pattern search algorithm [38] at the cost of 1,030 low-fidelity model evaluations per point (the cost includes the function evaluations to fix C_l).

In the next step, a Kriging interpolation model $\boldsymbol{s}_{KR}$ has been set up using 600 (2,805 low-fidelity function evaluations) training points allocated using Latin Hypercube Sampling (LHS) [22]. The initial approximation of the Pareto front has been obtained by optimizing $\boldsymbol{s}_{KR}$ using MOEA (cf. Section 2.3). The initial Pareto front representation is shown in Fig. 4. Finally, 10 designs sampled along the initial front have been refined using the procedure of Section 2.4 (cf. (2)). The final representation of the Pareto front has been obtained in two refinement iterations. The termination condition for the refinement process was drag modification of the refined samples less than two drag counts (1 drag count is defined as $\Delta C_d = 10^{-4}$). The initial and refined high-fidelity Pareto-optimal solutions are also shown in Fig. 4. The cost of the refinement process was 60 evaluations of the high-fidelity model $\boldsymbol{f}$ and 740 evaluations of the low-fidelity model $\boldsymbol{c}$. Thus the overall cost of the multi-objective design in this case corresponds to only about 243 evaluations of $\boldsymbol{f}$. The cost of multi-objective optimization of the Kriging surrogate can be neglected. In order to get an idea about computational savings obtained with the proposed approach, it should be noted that the surrogate model optimization by MOEA required 20,000 objective function evaluations (population size 200, maximum number of iterations 100). Although direct high-fidelity model optimization with MOEA is prohibitive, the above figures provide an estimated computational savings, which are tremendous (around two orders of magnitude).

The Pareto front, as shown in Fig. 4, illustrates the best possible trade-offs between the drag and pitching moment coefficients. For further analysis, we only consider the part of the Pareto front for which the drag coefficient is lower than 0.015, and representation of which contains eight designs. Starting from the lower pitching moment as the first design, we consider the first, third, fifth and seventh design and analyze them in more detail. Their corresponding pressure coefficient distributions and airfoil shapes, and Mach contours are shown in Figs. 5 and 6, respectively. In all the selected designs there are two strong shocks near the leading edge and at around 0.5 chord location.

The airfoil shapes are thinner at the leading edge. In particular, there is a big reduction in thickness in the lower surface of the airfoils (Fig. 5). The pressure coefficient distributions shape, and shock locations are similar in all designs. However

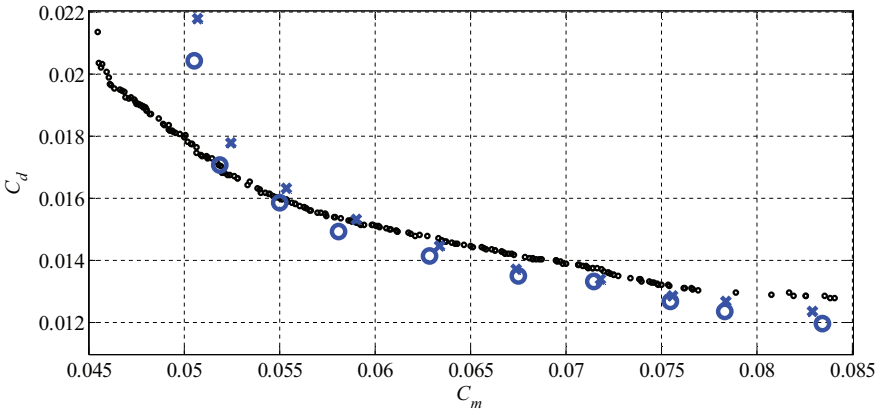

Fig. 4. Pareto sets for design case I: initial approximation of the Pareto front obtained by optimizing the Kriging surrogate (small circles), 10 high-fidelity model designs sampled along the front (×), and 10 refined high-fidelity model samples (O).

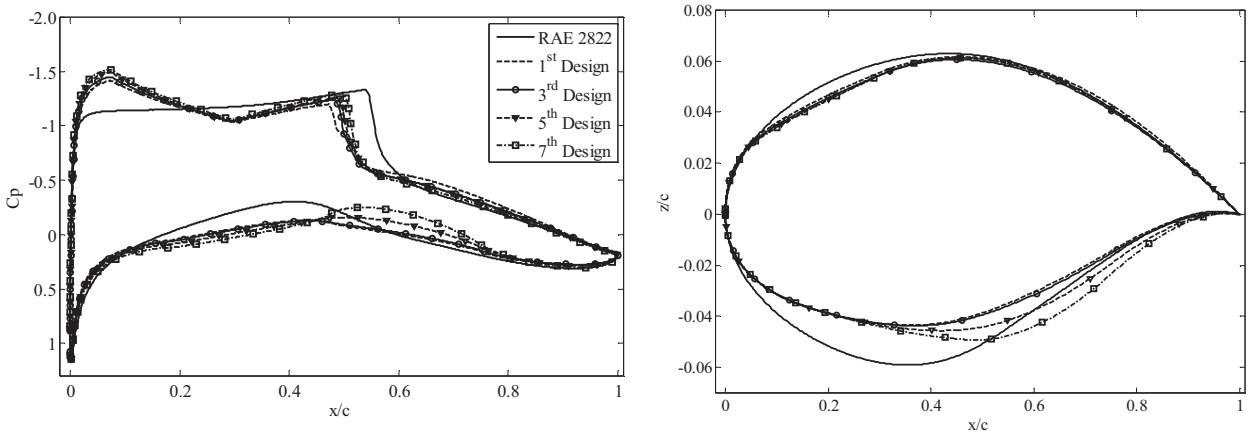

Fig. 5. Pressure coefficient distributions and airfoil shapes of the reference and the designs selected from the Pareto front for design case I.

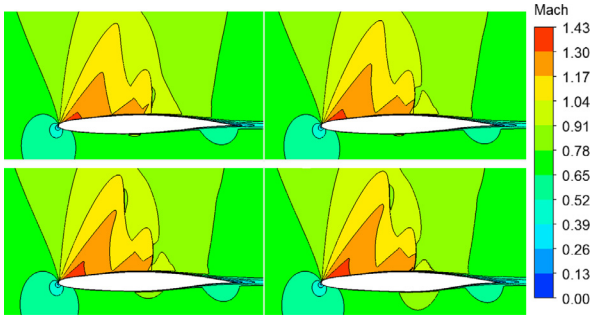

Fig. 6. Mach contours for the selected designs from the top left corner and to the bottom right corner (clockwise) - 1st design, 3rd design, 5th design and 7th design of design case I.

the shock strengths are different in magnitudes. As it can be clearly seen from Figs. 5 and 6, the shock strength is increasing as the pitching moment is increasing, and the shock location almost fixed near the leading edge and at around 0.5 chord location.

3.4. Numerical results: design case II

The extreme point of the Pareto front obtained at the level of the low-fidelity CFD model obtained for the second design case (B-spline parameterization with 12 design variables at fixed lift, $C_{l.target}=0.824$) are as follows: drag minimization, $\boldsymbol{x}_c^{*(1)}=[0.0151\ 0.0410\ 0.0591\ 0.0631\ 0.0643\ 0.0238\ -0.0086\ -0.0540\ -0.0282\ -0.0416\ -0.0248\ 0.0104]^T$, $C_l=0.8235$,

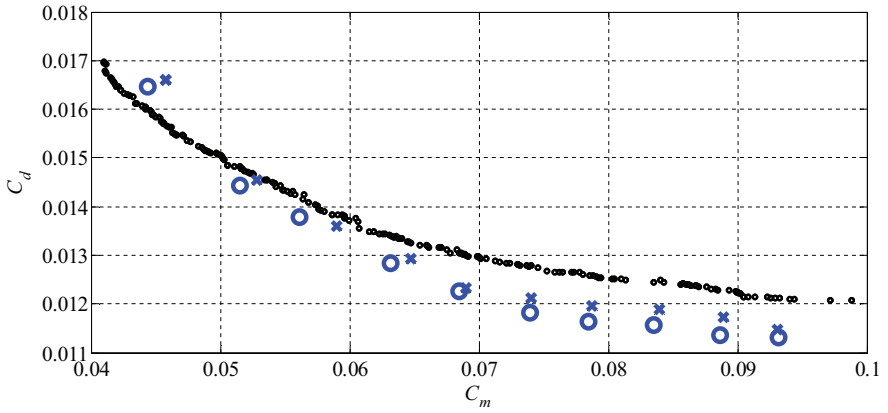

Fig. 7. Pareto sets for design case II: initial approximation of the Pareto front obtained by optimizing the Kriging surrogate (small circles), 10 high-fidelity model designs sampled along the front (×), and 10 refined high-fidelity model samples (O).

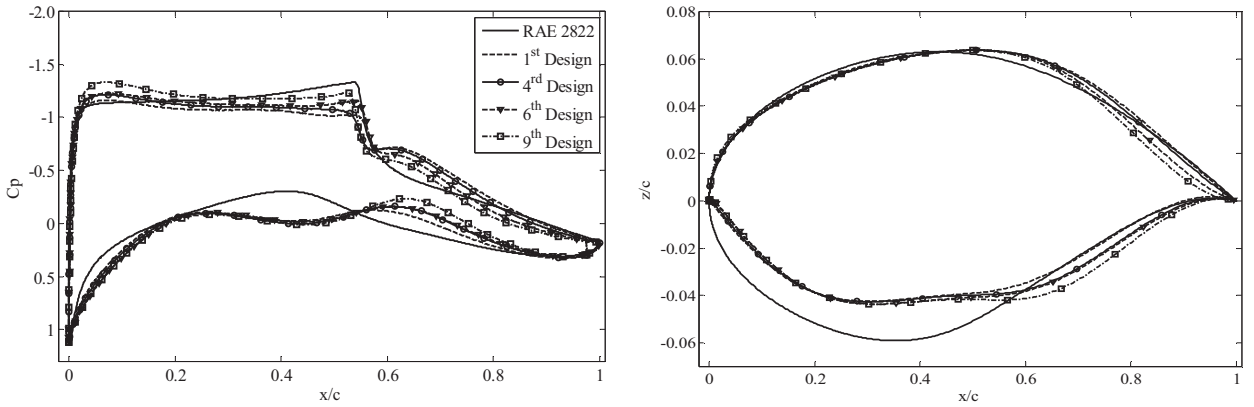

Fig. 8. Pressure coefficient distributions and airfoil shapes of the reference and the designs selected from the Pareto front for design case II.

$C_d = 0.0121$, $C_m = -0.1200$, and pitching moment maximization $\boldsymbol{x}_c^{*(2)} = [0.0240\ 0.0452\ 0.0625\ 0.0663\ 0.0725\ 0.0004\ 0.0114\ -0.0473\ -0.0612\ -0.0436\ -0.0507\ 0.0035]^T$, $C_l = 0.8235$, $C_d = 0.0186$, $C_m = -0.0438$.

In this case, we are only interested in the part of the Pareto front for which the drag coefficient is not larger than 0.0150. The reduced design space (according to Section 2.2) is therefore defined by the following bounds: $\boldsymbol{l}^* = [0.0240\ 0.0452\ 0.0625\ 0.0663\ 0.0725\ 0.0004\ 0.0114\ -0.0473\ -0.0612\ -0.0436\ -0.0507\ 0.0035]^T$ and $\boldsymbol{u}^* = [0.0151\ 0.0410\ 0.0591\ 0.0631\ 0.0643\ 0.0238\ -0.0086\ -0.0540\ -0.0282\ -0.0416\ -0.0248\ 0.0104]^T$. It is over 10^8 times smaller (volume-wise) than the original space. The extreme points were obtained using the pattern search algorithm [38] at the cost of 600 low-fidelity model evaluations per point (the cost includes the function evaluations to fix C_l).

In the next step, a Kriging interpolation model $\boldsymbol{s}_{KR}$ has been set up using 900 (4,144 low-fidelity function evaluations) training points allocated using Latin Hypercube Sampling (LHS) [22]. The initial approximation of the Pareto front has been obtained by optimizing $\boldsymbol{s}_{KR}$ using MOEA (cf. Section 2.3). The initial Pareto front representation is shown in Fig. 7. Finally, 10 designs sampled along the initial front have been refined using the procedure of Section 2.4 (cf. (2)). The final representation of the Pareto front has been obtained in one refinement iteration, which was sufficient because of a very good quality of the Kriging surrogate (with respect to the low-fidelity CFD model). The termination condition for the refinement process was the same as for the first case: drag modification of the refined samples less than two drag counts. The initial and refined high-fidelity Pareto-optimal solutions are also shown in Fig. 7. The cost of the refinement process was 60 evaluations of the high-fidelity model $\boldsymbol{f}$ and 1,060 evaluations of the low-fidelity model $\boldsymbol{c}$. Thus the overall cost of the multi-objective design in this case corresponds to only about 274 evaluations of $\boldsymbol{f}$.

The Pareto front, as shown in Fig. 7, illustrates the best possible trade-offs between the drag and pitching moment coefficients. For further analysis, we only consider the part of the Pareto front for which the drag coefficient is lower than 0.015, and representation of which contains nine designs. Starting from the lower pitching moment as the first design, we consider the first, fourth, sixth and ninth design and analyze them in more detail. Their corresponding pressure coefficient distributions and airfoil shapes, and Mach contours are shown in Figs. 8 and 9, respectively.

As it can be clearly observed from Figs. 8 and 9, the shock strength is increasing as the pitching moment is increasing, however the shock location and pressure coefficient distributions shape are similar in all designs. In general the airfoil shapes are thinner at the lower surface of leading edge as compared to the baseline airfoil. The other trend that can be seen

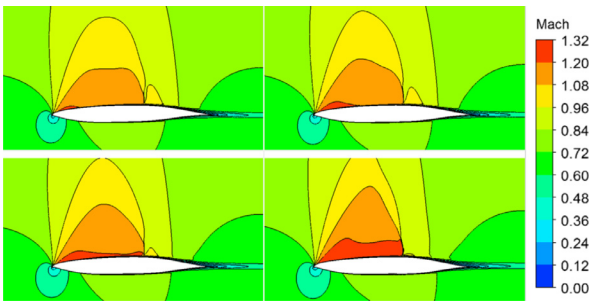

Fig. 9. Mach contours for the selected designs from the top left corner and to the bottom right corner (clockwise) - 1st design, 4th design, 6th design and 9th design of design case II.

is that as we move from the lower pitching moment towards the higher one, near the trailing edge of the lower surface, the thickness is increasing, and it is vice-versa near the trailing edge of the upper surface. In addition, on the upper surface there is no big change in thickness near the leading edge.

4. Conclusion

Expedited multi-objective constrained design optimization of transonic airfoils has been presented. Our approach exploits variable-fidelity CFD simulations and auxiliary surrogate model created from Kriging-interpolated low-fidelity CFD simulation data. An initial approximation of the Pareto front is identified using a multi-objective evolutionary algorithm, and it is further refined by means of response correction techniques and local response surface approximation models. Design constraints are handled at the level of multi-objective evolutionary algorithm by appropriate modifications of the recombination and mutation operators. Determination of the angle of attack ensuring the target lift coefficient is accelerated by reusing the low-fidelity CFD model data, originally acquired for Kriging model construction.

The two application case studies involving low-dimensional design spaces (up to 12 design variables) provided in the paper demonstrate that our methodology is capable of finding a set of designs representing the best trade-offs between design objectives, here, drag minimization and pitching moment maximization, at a low cost corresponding to less than three hundred evaluations of the high-fidelity CFD model of the respective airfoil. This cost is dramatically lower than the cost of direct optimization of the high-fidelity model. The computational savings can be estimated to be around two orders of magnitude compared to conventional multi-objective optimization using population-based metaheuristics. In particular, the proposed approach renders multi-objective optimization using high-fidelity models computationally tractable.

It should be mentioned that the optimization methodology considered here is not general. As its foundation is reduction of the design space (in the sense of narrowing down the lower and upper bounds for design variables), certain assumptions have to be satisfied concerning the geometry of the Pareto front, in particular, that it is (or at least the most of it) contained in the reduced space. While it may not be the case in general, for the class of problems considered in this work, the Pareto front is normally a connected set which is allocated relatively close to the line segment connecting the extreme Pareto-optimal solutions (defining the reduced space), which allows for identifying the majority of the Pareto front by the proposed method.

Future work will be focused on extending the approach for medium-dimensional (between 10 to 40 design variables) to high-dimensional cases (over 40 design variables), as well as handling more demanding applications such as three-dimensional wing design.

Acknowledgments

Y. A. Tesfahunegn has received funding from the People Programme (Marie Curie Actions) of the European Union's Seventh Framework Programme FP7/2007-2013/under REA Grant agreement no. PIEF-GA-2012-331454.

References

[1] K. Leoviriyakit, S. Kim, A. Jameson, Viscous aerodynamic shape optimization of wings including planform variables, in: Proceedings of the 21st Applied Aerodynamics Conference, Orlando, Florida, 2003 June 23-26.
[2] R.A. Braembussche, Numerical optimization for advanced turbomachinery design, in: D. Thevenin, G. Janiga (Eds.), Optimization and Computational Fluid Dynamics, Springer, 2008, pp. 147–189.
[3] C.A. Mader, J.R.R.A. Martins, Derivatives for time-spectral computational fluid dynamics using an automatic differentiation adjoint, AIAA J. 50 (12) (2012) 2809–2819.
[4] A. Mousavi, S. Nadarajah, Heat transfer optimization of gas turbine blades using an adjoint approach, in: Proceedings of the 13th AIAA/ISSMO Multidisciplinary Analysis Optimization Conference, Fort Worth, Texas, 2010 Sept. 13-15.
[5] T.M. Leung, D.W. Zingg, Aerodynamic shape optimization of wings using a parallel Newton–Krylov approach, AIAA J. 50 (3) (2012) 540–550.
[6] B. Epstein, S. Peigin, Constrained aerodynamic optimization of three-dimensional wings driven by Navier–Stokes computations, AIAA J. 43 (9) (2005) 1946–1957.

[7] J. Nocedal, S.J. Wright, Numerical Optimization, Springer, 2006.
[8] S. Kim, K. Hosseini, K. Leoviriyakit, A. Jameson, Enhancement of class of adjoint design methods via optimization of parameters, AIAA J. 48 (6) (2010) 1072–1076.
[9] S. Schmidt, N. Gauger, C. Ilic, V. Schulz, Three dimensional large scale aerodynamic shape optimization based on shape calculus, in: Proceedings of the 41st AIAA Fluid Dynamics Conference and Exhibit, Honolulu, Hawaii, 2011 June 27-30.
[10] N.V. Queipo, R.T. Haftka, W. Shyy, T. Goel, R. Vaidyanathan, P.K. Tucker, Surrogate-based analysis and optimization, Prog. Aerosp. Sci. 41 (1) (2005) 1–28..
[11] A.I.J. Forrester, A.J. Keane, Recent advances in surrogate-based optimization, Prog. Aerosp. Sci. 45 (1–3) (2009) 50–79.
[12] S. Koziel, D. Echeverría-Ciaurri, L. Leifsson, Surrogate-based methods, in: S. Koziel, X.S. Yang (Eds.), Computational Optimization, Methods and Algorithms, Series: Studies in Computational Intelligence, Springer-Verlag, 2011, pp. 33–60.
[13] N.M. Alexandrov, R.M. Lewis, C.R. Gumbert, L.L. Green, P.A. Newman, Optimization with variable-fidelity models applied to wing design, in: Proceedings of the 38th Aerospace Sciences Meeting & Exhibit, Reno, NV, 2000 AIAA Paper 2000-0841 Jan.
[14] T.D. Robinson, M.S. Eldred, K.E. Willcox, R. Haimes, Surrogate-based optimization using multifidelity models with variable parameterization and corrected space mapping, AIAA J. 46 (11) (2008).
[15] A.J. Booker, J.E. Dennis Jr., P.D. Frank, D.B. Serafini, V. Torczon, M.W. Trosset, A rigorous framework for optimization of expensive functions by surrogates, Struct. Opt. 17 (1) (1999) 1–13.
[16] C.M. Fonseca, Multiobjective Genetic Algorithms with Applications to Control Engineering Problems (Ph.D thesis), Department of Automatic Control and Systems Engineering, University of Sheffield, Sheffield, UK, 1995.
[17] C.A. Coello Coello, G.B. Lamont, Applications of Multi-Objective Evolutionary Algorithms, World Scientific, 2004.
[18] B. Epstein, S. Peigin, Robust hybrid approach to multiobjective constrained optimization in aerodynamics, AIAA J. 42 (8) (2004) 1572–1581.
[19] M. Nemec, D.W. Zingg, T.H. Pulliam, Multipoint and multi-objective aerodynamic shape optimization, AIAA J. 42 (6) (2004) 1057–1065.
[20] S. Koziel, L. Leifsson, Knowledge-based airfoil shape optimization using space mapping, in: Proceedings of the 30th AIAA Applied Aerodynamics Conference, New Orleans, Louisiana, 2012 June 25–28.
[21] S. Koziel, Q.S. Cheng, J.W. Bandler, Space mapping, IEEE Microw. Mag. 9 (6) (2008) 105–122.
[22] B. Beachkofski, R. Grandhi, Improved distributed hypercube sampling, in: Proceedings of the AIAA Paper 2002-1274, 43rd AIAA/ASME/ASCE/AHS/ASC Structures, Structural Dynamics, and Materials Conference, Denver, CO, 2002 April 22–25.
[23] ICEM CFD, ver. 14.0, ANSYS Inc., Southpointe, 275 Technology Drive, Canonsburg, PA 15317, 2012.
[24] FLUENT, ver. 14.0, ANSYS Inc., Southpointe, 275 Technology Drive, Canonsburg, PA 15317, 2012.
[25] A. March, W. Willcox, Provably convergent multifidelity optimization algorithm not requiring high-fidelity derivatives, AIAA J. 50 (5) (2012) 1079–1089.
[26] A. March, W. Willcox, Constrained multifidelity optimization using model calibration, Struct. Multidiscip. Optim. 46 (2012) 93–109.
[27] Z.-H. Han, S. Gortz, R. Hain, A variable-fidelity modeling method for aero-loads prediction, Notes Numer. Fluid Mech. Multidiscip. Des. 112 (2010) 17–25.
[28] Z.-H. Han, S. Gortz, R. Zimmermann, On improving efficiency and accuracy of variable-fidelity surrogate modeling in aero-data for loads context, in: Proceedings of the CEAS 2009 European Air and Space Conference, Manchester, UK, October 26-29 2009, London, UK: Royal Aeronautical Society.
[29] Z.-H. Han, R. Zimmermann, S. Gortz, A new cokriging method for variable-fidelity surrogate modeling of aerodynamic data, in: Proceedings of the 48th AIAA Aerospace Sciences Meeting Including the New Horizons Forum and Aerospace Exposition, Orlando, FL, 2010 January 4-7AIAA 2010-1225.
[30] J.W. Bandler, Q.S. Cheng, S. Dakroury, A.S. Mohamed, M.H. Bakr, K. Madsen, J. Sondergaard, Space mapping: the state of the art, IEEE Trans. Microw. Theory Tech. 52 (1) (2004) 337–361 January.
[31] S. Koziel, L. Leifsson, Surrogate-based aerodynamic shape optimization by variable-resolution models, AIAA J. 51 (1) (2013) 94–106.
[32] L. Leifsson, S. Koziel, Surrogate modeling and optimization using shape-preserving response prediction: a review, Eng. Optim. (2015) 1–21 May 6, doi:10.1080/0305215X.2015.1016509.
[33] S. Koziel, L Leifsson, Adaptive response correction for surrogate-based airfoil shape optimization, in: Proceedings of the 30th AIAA Applied Aerodynamics Conference, New Orleans, Louisiana, 2012 June 25-28.
[34] S. Koziel, L Leifsson, Multi-fidelity airfoil optimization with adaptive response prediction, in: Proceedings of the 14th AIAA/ISSMO Multidisciplinary Analysis and Optimization Conference, Sept. 17-19, Indianapolis, Indiana, 2012.
[35] A. Zerbinati, A. Minelli, I. Ghazlane, J.-A. Desideri, Meta-model-assisted MGDA for multi-objective functional optimization, Comput. Fluids 102 (10) (2014) 116–130.
[36] G. Farin, Curves and Surfaces for Computer Aided Geometric Design, Academic Press, Boston, MA, 1993.
[37] D.W. Kinsey, T.J. Barth, Description of a Hyperbolic Grid Generation Procedure for Arbitrary Two-Dimensional Bodies, AFWAL TM 84-191-FIMM, 1984.
[38] S. Koziel, Computationally efficient multi-fidelity multi-grid design optimization of microwave structures, Appl. Comput. Electromagn. Soc. J. 25 (7) (2010) 578–586.
[39] K.C. Tan, E.F. Khor, T.H. Lee, Multiobjective Evolutionary Algorithms and Applications, Springer-Verlag, 2005.
[40] L. Leifsson, S. Koziel, Y.A. Tesfahunegn, S. Hosder, J.-R. Gramanzini, Aerodynamic design optimization: physics-based surrogate approaches for airfoil and wing design, in: Proceedings of the AIAA 52nd Aerospace Sciences Meeting, National Harbor, Maryland, 2014 January 13-17.
[41] Y.A. Tesfahunegn, A. Koziel, J.-R. Gramanzini, S. Hosder, Z.-H. Han, L. Leifsson, Direct and surrogate-based optimization of benchmark aerodynamic problems: a comparative study, in: Proceedings of the 53rd AIAA Aerospace Sciences Meeting, Science and Technology Forum, Kissimee, Florida, 2015 Jan 5-9.